

Proximal Gradient Descent Unfolding Dense-spatial Spectral-attention Transformer for Compressive Spectral Imaging

Ziyan Chen*

School of Automation, Guangdong University of Technology

zychen@gdut.edu.cn

Jing Cheng

School of Physics, South China University of Technology

phjcheng@scut.edu.cn

Abstract

The Coded Aperture Snapshot Spectral Compressive Imaging (CASSI) system modulates three-dimensional hyperspectral images into two-dimensional compressed images in a single exposure. Subsequently, three-dimensional hyperspectral images (HSI) can be reconstructed from the two-dimensional compressed measurements using reconstruction algorithms. Among these methods, deep unfolding techniques have demonstrated excellent performance, with RDLUF-Mix S^2 achieving the best reconstruction results. However, RDLUF-Mix S^2 requires extensive training time, taking approximately 14 days to train RDLUF-Mix S^2 -9stg on a single RTX 3090 GPU, making it computationally expensive. Furthermore, RDLUF-Mix S^2 performs poorly on real data, resulting in significant artifacts in the reconstructed images. In this study, we introduce the Dense-spatial Spectral-attention Transformer (DST) into the Proximal Gradient Descent Unfolding Framework (PGDUF), creating a novel approach called Proximal Gradient Descent Unfolding Dense-spatial Spectral-attention Transformer (PGDUDST). Compared to RDLUF-Mix S^2 , PGDUDST not only surpasses the network reconstruction performance limit of RDLUF-Mix S^2 but also achieves faster convergence. PGDUDST requires only 58% of the training time of RDLUF-Mix S^2 -9stg to achieve comparable reconstruction results. Additionally, PGDUDST significantly alleviates the artifact issues caused by RDLUF-Mix S^2 in real experimental data, demonstrating superior performance and producing clearer reconstructed images.

1. Introduction

Hyperspectral images (HSIs), consisting of numerous continuous and narrow spectral bands, provide a more comprehensive depiction of the observed scene compared to standard RGB images. Leveraging their inherently rich and detailed spectral characteristics, HSIs find extensive use in various computer vision tasks and graphical applications, including medical imaging [28, 30, 52], image classification [27, 34, 55], remote sensing [21, 42, 45, 51], object tracking [31, 50, 61, 69], and more. To obtain HSIs, conventional imaging systems equipped with spectrometers scan scenes in either the spatial or spectral dimension, often requiring a considerable amount of time [19]. Consequently, these traditional imaging systems fail to capture and measure dynamic scenes. Recently, snapshot compressive imaging (SCI) systems [8, 12, 16, 33, 53, 54, 64] have been developed to capture HSIs. These SCI systems modulate the three-dimensional (3D) hyperspectral image along the spectral dimension into a single two-dimensional (2D) compressive image. Among these SCI systems, coded aperture snapshot spectral imaging (CASSI) [1, 20, 26, 37, 56] stands out due to its remarkable performance. CASSI acquires a spectral image by employing a coded aperture and dispersive components to modulate the spectral content within the scene. By capturing a 2D compressed measurement of the 3D data cube, the CASSI technique offers an efficient approach to acquiring spectral data. Nevertheless, reconstructing the 3D HSI cube from the 2D measurements presents a fundamental challenge for the CASSI system.

Based on CASSI, various reconstruction techniques can be categorized into four groups: model-based techniques [17, 29, 32, 49, 53, 57, 67], Plug-and-play (PnP) algorithms [10, 39, 46, 63, 65], end-to-end (E2E) approaches [4, 5, 23, 37, 38, 40], and deep unfolding methods [7, 15, 18, 25, 35, 36, 58, 59, 68]. Model-based techniques rely on manually defined priors

and assumptions, leading to limited generality and slow reconstruction speed. PnP algorithms integrate pre-trained denoising networks into traditional model-based methods, but the fixed nature of the pre-trained networks limits their performance. E2E methods learn the mapping function from measurements to HSIs using deep learning, but they often lack theoretical properties, interpretability, and flexibility due to differences in hardware systems. Deep unfolding methods use a multi-stage network to map measurements to the HSI cube, providing interpretability and deep learning capabilities, making them promising for HSI reconstruction. Among these methods, deep unfolding methods have shown superior performance by converting traditional iterative optimization algorithms into a series of deep neural network (DNN) blocks.

Among these deep unfolding methods, the reconstruction quality of RDLUF-Mix S^2 [15] stands out as the best. RDLUF-Mix S^2 [15] consists of two main modules: the Residual Degradation Learning Unfolding Framework (RDLUF), which integrates the residual degradation learning strategy into the data subproblem of Proximal Gradient Descent (PGD) [2], and the Mixing priors across Spatial and Spectral (Mix S^2) Transformer, integrated into RDLUF as the denoiser for the prior subproblem. While RDLUF-Mix S^2 exhibits the best reconstruction performance among these approaches, boasting an impressive average PSNR of 39.57 dB for reconstructed images, it faces the challenge of longer training time. Achieving optimal reconstruction results with RDLUF-Mix S^2 requires approximately 14 days of training on a single RTX 3090 GPU, making it computationally expensive. Furthermore, RDLUF-Mix S^2 shows suboptimal performance with real experimental data, leading to reconstructed images containing significant artifacts.

In this paper, we introduce a novel Dense-spatial Spectral-attention Transformer (DST) and integrate it into the Proximal Gradient Descent Unfolding Framework (PGDUF), presenting a new method named Proximal Gradient Descent Unfolding Dense-spatial Spectral-attention Transformer (PGDUDST). PGDUF combines a deep unfolding framework with proximal gradient descent algorithms, gradually approximating the original high-dimensional data through multiple iterative stages. Each stage comprises a gradient descent module (primarily used to estimate residuals between the sensing matrix and the degradation matrix) and a proximal mapping module (DST), with the goal of enhancing adaptability to changes in the sensing matrix and improving reconstruction performance through multi-stage approximation. The proposed DST incorporates parallel-designed mechanisms, including Dense-spatial and Spectral-attention, enhancing the model's ability to capture complex details and structures. To further strengthen modeling capabilities in both spectral and spatial dimensions, a mechanism for bidirectional interaction of information in spatial and spectral domains is introduced. Additionally, the Dense-spatial mechanism combines Lightweight Inception and DenseBlock in a novel way, leveraging the strengths of both architectures. This combination excels in feature extraction, information aggregation, and gradient flow, thereby enhancing the overall performance of the model and achieving rapid convergence. Compared to RDLUF-Mix S^2 , our proposed method, PGDUDST, exhibits three key advantages:

- (1) PGDUDST achieves reconstruction results comparable to RDLUF-Mix S^2 -9stg but with a training time that is only 58% of RDLUF-Mix S^2 -9stg, resulting in nearly halved training time.
- (2) PGDUDST surpasses the network reconstruction limit of RDLUF-Mix S^2 .
- (3) PGDUDST demonstrates superior performance with real experimental data, effectively mitigating the prominent artifacts found in RDLUF-Mix S^2 and yielding a cleaner and more detailed reconstruction in real-world experimental scenarios.

2. The CASSI system

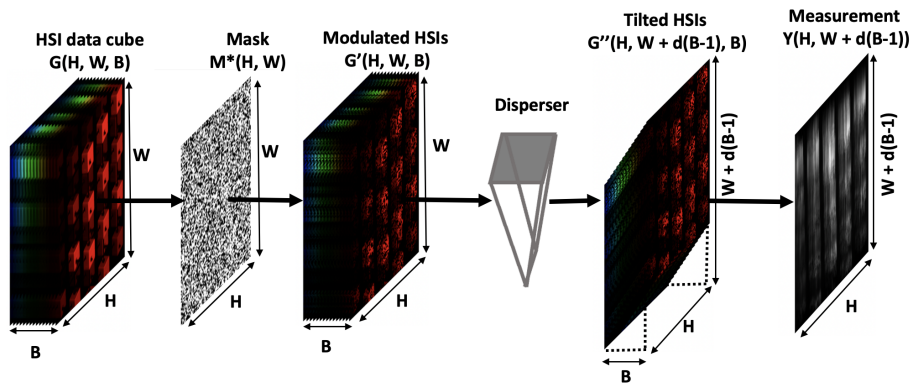


Figure 1. The schematic of the CASSI system.

A concise CASSI system is illustrated in Fig.1. The 3D HSI data cube is denoted as $\mathbf{G} \in \mathbb{R}^{H \times W \times B}$, where H , W , and B represent the height, width, and number of wavelengths of the 3D HSI, respectively. A physical mask $\mathbf{M} \in \mathbb{R}^{H \times W}$ is utilized to modulate the 3D HSI \mathbf{G} . Each channel of this 3D HSI \mathbf{G} is modulated by this physical mask, and this process can be expressed in mathematical formulas as follows:

$$\mathbf{G}'(:, :, b) = \mathbf{G}(:, :, b) \odot \mathbf{M} \quad (1)$$

where \odot represents element-wise multiplication, $b \in [1, 2, 3, \dots, B]$, and $\mathbf{G}' \in \mathbb{R}^{H \times W \times B}$ is the modulated 3D HSI. Consequently, the modulated 3D HSI \mathbf{G}' is shifted by the disperser, expressed as:

$$\mathbf{G}''(h, w, b) = \mathbf{G}'(h, w + d(b - 1), b) \quad (2)$$

Here, $\mathbf{G}'' \in \mathbb{R}^{H \times (W + d(B - 1)) \times B}$ represents the tilted 3D HSI, which is shifted from \mathbf{G}' , and d represents the shifting step. Finally, the 2D compressed measurement $\mathbf{Y} \in \mathbb{R}^{H \times [W + d(B - 1)]}$ can be obtained by

$$\mathbf{Y} = \sum_{b=1}^B \mathbf{G}''(:, :, b) + \mathbf{N} \quad (3)$$

where $\mathbf{N} \in \mathbb{R}^{H \times [W + d(B - 1)]}$ represents the noise of the CASSI system.

Meanwhile, the degradation model of the CASSI system can be formulated as

$$y = Ag + n, \quad (4)$$

where $g \in \mathbb{R}^{HWB \times 1}$ is reshaped from the 3D HSI $\mathbf{G} \in \mathbb{R}^{H \times W \times B}$, $y \in \mathbb{R}^{H[W + d(B - 1)] \times 1}$ is reshaped from the modulated imaging speckle patterns $\mathbf{Y} \in \mathbb{R}^{H \times [W + d(B - 1)]}$ captured by the camera, $n \in \mathbb{R}^{H[W + d(B - 1)] \times 1}$ is reshaped from the noise \mathbf{N} of the CASSI system. $A \in \mathbb{R}^{H[W + d(B - 1)] \times HWB}$ represents the sensing matrix calibrated based on pre-design.

3. Method

3.1. The Proximal Gradient Descent algorithm

Reconstructing the high-quality image g from the compressed measurement y is typically an ill-posed problem. Based on the maximizing the posterior probability (MAP) theory, Eq.4 can be solved as

$$\hat{g} = \underset{g}{\operatorname{argmin}} \frac{1}{2} \|y - Ag\|^2 + \tau J(g), \quad (5)$$

where $\frac{1}{2} \|y - Ag\|^2$ represents the data fidelity term, $J(g)$ corresponds to the image prior term, and τ is a hyperparameter that balances their relative importance. The PGD algorithm approximately formulates Eq.5 as an iterative convergence problem using the following iterative function:

$$\hat{g}^k = \underset{g}{\operatorname{argmin}} \frac{1}{2\beta} \|g - (\hat{g}^{k-1} - \beta A^T(A\hat{g}^{k-1} - y))\|^2 + \tau J(g), \quad (6)$$

where \hat{g}^k is the output of the k -th iteration, and β represents the step size.

Mathematically, the provided function consists of two main components: the blue part involves a gradient descent operation, and the red part can be addressed through the proximal operator $\operatorname{proj}_{\tau, J}$. This formulation results in a data subproblem and a prior subproblem, specifically gradient descent (Eq.7a) and proximal mapping (Eq.7b):

$$v^k = \hat{g}^{k-1} - \beta A^T(A\hat{g}^{k-1} - y) \quad (7a)$$

$$\hat{g}^k = \operatorname{proj}_{\tau, J}(v^k) \quad (7b)$$

The PGD algorithm iteratively updates v^k and \hat{g}^k until convergence.

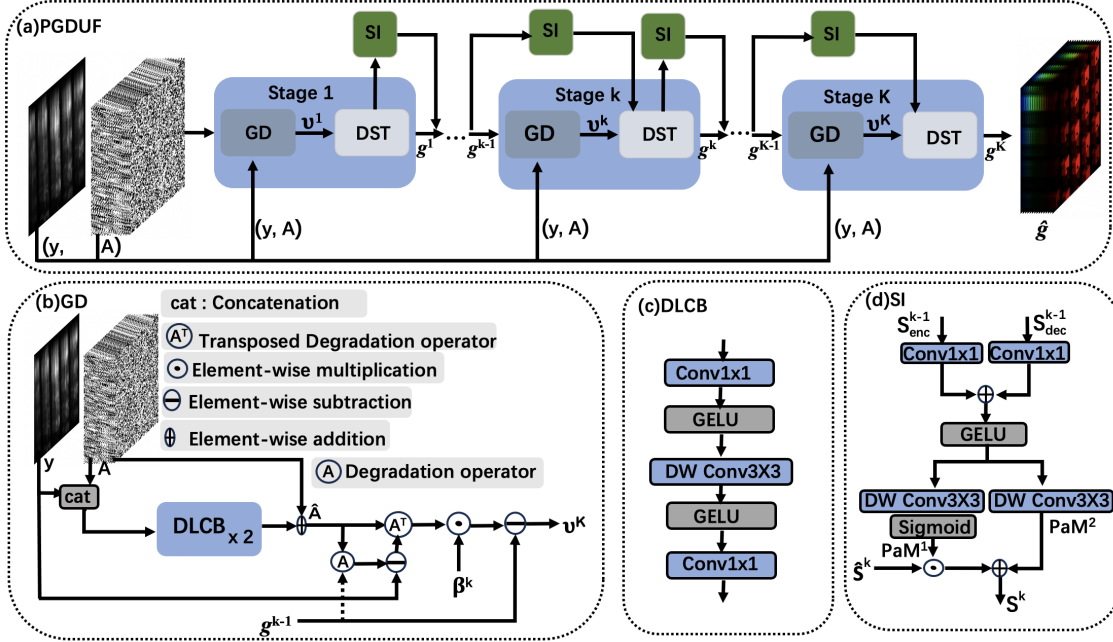


Figure 2. (a)The architecture of the proposed PGDUF with K stages (iterations). (b) Gradient Descent module (GD). (c) Degradation Learning Convolution Block (DLCB). (d)Stage Interaction module (SI).

3.2. Proximal Gradient Descent Unfolding Framework

Our proposed framework, PGDUF, is illustrated in Fig. 2, representing a deep unfolding framework based on the Proximal Gradient Descent algorithm. PGDUF comprises several iteratively applied stages, each featuring a Gradient Descent module and a Proximal Mapping module. These modules correspond to the gradient descent (Eq.7a) and proximal mapping (Eq.7b) steps within a single iteration of the PGD algorithm. From a Bayesian perspective, the PM module can be interpreted as addressing a denoising problem [10, 63]. As depicted in Fig. 2(a), we have developed the Dense-spatial Spectral-attention Transformer (DST) as the PM module, and further details about DST will be illustrated in the upcoming subsection. Additionally, between each pair of adjacent stages, stage interaction has been introduced to enhance features and stabilize optimization through spatial adaptive normalization.

Gradient Descent module. The Gradient Descent module employed in this work follows the one in the study [15]. This module estimates the residual between the sensing matrix A and the degradation matrix \hat{A} , and its architecture is depicted in Fig. 2(b). The GD module comprises two inputs: one is the compressed measurement y , and the other is the sensing matrix A . It consists of two Degradation Learning Convolution Blocks (DLCBs), whose architecture is also presented in Fig. 2(c). The gradient descent step in the GD module can be expressed as follows:

$$v^k = \hat{g}^{k-1} - \beta^k \hat{A}^T (\hat{A} \hat{g}^{k-1} - y) \quad (8)$$

in which β is a learnable parameter, k represents the number of stages, and the degradation matrix \hat{A} can be calculated as $\hat{A} = A + T_{DLCB}(\text{Concat}(y, A))$, where T_{DLCB} represents two cascaded DLCBs, and Concat denotes concatenation.

Stage Interaction module. The stage interaction module employs a Spatial Adaptive Normalization (SPAN) approach to normalize features at the current stage[15, 41, 44]. SPAN utilizes features from the previous stage to generate modulation parameters, and the computation of modulation parameters is expressed as follows:

$$\begin{aligned} \text{PaM}^1 &= \text{Sigmoid}\{\text{DWConv}[\text{GELU}[\text{Conv}(S_{enc}^{k-1}) + \text{Conv}(S_{dec}^{k-1})]]\} \\ \text{PaM}^2 &= \text{DWConv}[\text{GELU}[\text{Conv}(S_{enc}^{k-1}) + \text{Conv}(S_{dec}^{k-1})]] \end{aligned} \quad (9)$$

Here, k denotes the current stage number, PaM^1 (PaM^2) represents the generated modulation parameter of the current stage, and S_{enc}^{k-1} (S_{dec}^{k-1}) denotes the encoder (decoder) features from the previous stage. Subsequently, the features of the current stage are modulated as follows:

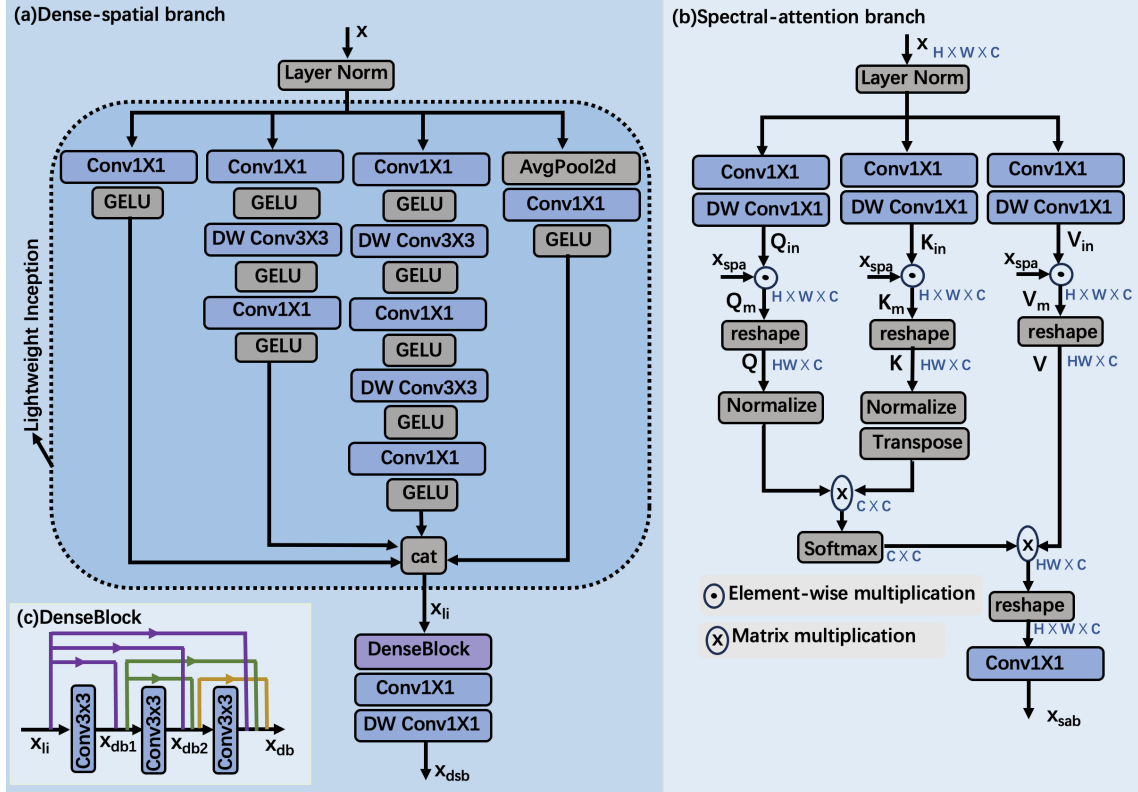


Figure 4. (a)Dense-spatial Branch. (b) Spectral-attention Branch. (c) DenseBlock.

In this section, we provide a comprehensive exposition of the proposed Dense-spatial Spectral-attention Transformer (DST).

Network Architecture. Illustrated in Fig.3(a), the DST employs a U-shaped structure with three hierarchical levels, comprising multiple foundational units referred to as Dense-spatial Spectral-attention blocks. To mitigate information loss resulting from up and down sampling operations, we introduce block interaction. This process entails the interpolation of features at different scales to a unified scale within each block interaction. Initially, the DST employs a Conv1 × 1 operation to map v^k to shallow features $G_0 \in \mathbb{R}^{H \times \hat{W} \times B}$, where $\hat{W} = W + d(B - 1)$. Subsequently, G_0 traverses through all Dense-spatial Spectral-attention blocks and block interactions, becoming embedded in deep features $G_d \in \mathbb{R}^{H \times \hat{W} \times B}$. Finally, a Conv1 × 1 operation is applied to G_d to generate the denoised image g_k .

Block Interaction. The Block Interaction module is depicted in Fig.3(c) and is designed to mitigate potential information loss that often occurs when resizing images or feature maps in the field of deep learning, particularly through common up-sampling and down-sampling operations. The Block Interaction module interpolates features at various scales, consolidating them within each block interaction. As a result, this process efficiently minimizes information loss during size transformations. The output of the Block Interaction module can be expressed as follows:

$$B_O = \text{Conv}\{\text{GELU}(\text{Conv}(\text{Concat}(B_I, B_{I1}, B_{I2})))\} \quad (11)$$

where B_{Ii} ($i = 1, 2$) represents features that have been interpolated to the same scale as B_I .

Dense-spatial Spectral-attention Block. The key component of the DST is the Dense-spatial Spectral-attention block, illustrated in Fig.3(b). This block comprises a Dense-spatial branch and a Spectral-attention branch, incorporating bidirectional interaction between spatial and spectral dimensions. Additionally, it includes a detailed gated-Dconv feed-forward network [66] as depicted in Fig.3(d). The details of the Dense-spatial branch, Spectral-attention branch, and the Spectral-Spatial Bidirectional Interaction are described as follows.

Dense-spatial Branch. The Dense-spatial Branch is illustrated in Fig.4(a). The employed Lightweight Inception module adheres to the design principles outlined in [47, 48], incorporating a modification: the use of DWConv3 × 3 instead of Conv3 ×

3, as depicted in Fig.4(a) following [15]. Operating across various scales, the Lightweight Inception module processes visual information and aggregates it, allowing the subsequent layer to abstract features concurrently from different scales. This approach significantly enhances the network's capability to capture a broader spectrum of textures and details. Furthermore, the integration of the DenseBlock[24] module into the architecture, as depicted in Fig.4(c), further enhances the network's efficacy. The DenseBlock process is articulated as follows:

$$\begin{aligned} x_{db1} &= \text{Concat}(x_{li}, \text{Conv}(x_{li})) \\ x_{db2} &= \text{Concat}(x_{db1}, \text{Conv}(x_{db1})) \\ x_{db} &= \text{Concat}(x_{db2}, \text{Conv}(x_{db2})) \end{aligned} \quad (12)$$

Here, x_{li} represents the output of the Lightweight Inception module. DenseBlock structures facilitate feature reuse and promote gradient flow throughout the network, mitigating the vanishing gradient problem. This characteristic of DenseBlock modules is particularly advantageous in deep neural networks, enhancing the model's learning capacity and feature representation.

Following the Lightweight Inception module and the DenseBlock module, a sequence of operations, including $\text{Conv}1 \times 1$ and $\text{DWConv}1 \times 1$, is applied to generate the final output of the Dense-spatial Branch. The ultimate expression for the Dense-spatial Branch's output is defined as:

$$x_{dsb} = \text{DWConv}(\text{Conv}(x_{db})) \quad (13)$$

Here, x_{db} denotes the output of the DenseBlock module. The synergy of DenseBlock and Lightweight Inception harnesses the strengths of both architectures, resulting in a network that excels in feature extraction, information aggregation, and gradient flow, thereby enhancing the overall performance of the model and achieving rapid convergence.

Spectral-attention branch. The Spectral-attention branch follows the methodology outlined in [66], with its key component being the Spectral-wise Multi-head Self-Attention module (S-MSA) [5]. Fig. 4 (b) illustrates the Spectral-attention branch. The input x undergoes a Layer Norm layer to become x_{in} , which is then embedded through $\text{Conv}1 \times 1$ and $\text{DWConv}3 \times 3$ layers. This embedding process results in $Q_{in} = U_d^Q U_p^Q x_{in}$, $K_{in} = U_d^K U_p^K x_{in}$, and $V_{in} = U_d^V U_p^V x_{in}$, where $U_p^{(\cdot)}$ denotes $\text{Conv}1 \times 1$, and $U_d^{(\cdot)}$ denotes $\text{DW Conv}3 \times 3$. Subsequently, the obtained *query* (Q_{in}), *key* (K_{in}), and *value* (V_{in}) are element-wise multiplied with x_{spa} to yield

$$\begin{aligned} Q_m &= Q_{in} \odot x_{spa} \\ K_m &= K_{in} \odot x_{spa} \\ V_m &= V_{in} \odot x_{spa} \end{aligned} \quad (14)$$

Then, Q_m , K_m , and V_m are reshaped to obtain Q , K , and V , respectively, using the reshape operation, where $Q \in \mathbb{R}^{HW \times C}$, $K \in \mathbb{R}^{HW \times C}$, and $V \in \mathbb{R}^{HW \times C}$.

The final output of the Spectral-attention branch can be expressed as:

$$x_{sab} = \text{Conv}(\text{Reshape}(\text{Attention}(Q, K) \times W)) \quad (15)$$

Here, $\text{Attention}(Q, K) = \text{Softmax}\{\text{Normalize}(Q) \times \text{Transpose}(\text{Normalize}(K))\}$, and $\text{Attention}(Q, K) \in \mathbb{R}^{C \times C}$.

Spectral-Spatial Bidirectional Interaction. Having familiarity with [11], we introduce the Spectral-Spatial Bidirectional Interaction module. For spatial interaction, the output features x_{dsb} from the Dense-spatial Branch undergo $\text{Conv}1 \times 1$ to generate a spatial attention map, denoted as x_{spa} :

$$x_{spa} = \text{Conv}(x_{dsb}) \quad (16)$$

This spatial attention map x_{spa} is then applied to the *query* (Q_{in}), *key* (K_{in}), and *value* (V_{in}) in a spatial attention manner, as described in Eq. 14.

For spectral interaction, the output features x_{sab} from the Spectral-attention branch undergo a series of operations [22] to obtain a spectral attention weight map, denoted as x_{spe} :

$$x_{spe} = \text{Tile}(\text{Sigmoid}(\text{Conv}(\text{GELU}(\text{LN}(\text{Conv}(\text{AdaptiveAvgPool2d}(x_{sab}))))))) \quad (17)$$

Here, LN represents the Layer Norm layer. Subsequently, this spectral attention weight map x_{spe} is applied to the output features x_{dsb} of the Dense-spatial Branch in a spectral attention manner, resulting in the generation of the Spectral-Spatial attention map x_{spae} :

$$x_{spae} = x_{spe} \odot \text{GELU}(x_{dsb}) \quad (18)$$

4. Experiments

4.1. Experimental Settings

Following the configurations of TSA-Net [37], we utilize 28 wavelengths ranging from 450 nm to 650 nm, obtained through spectral interpolation manipulation, for HSIs. Our experiments cover both simulated and real HSI datasets.

Simulation HSI Data. We utilize two simulated HSI datasets, CAVE [43] and KAIST [14]. The CAVE dataset comprises 32 HSIs with a spatial size of 512×512, while the KAIST dataset includes 30 HSIs with a spatial size of 2704×3376. Following the methodology of TSA-Net [37], we designate CAVE as the training set. For testing purposes, we select 10 scenes from the KAIST dataset.

Real HSI Data. We employ the real HSI dataset obtained through the CASSI system, as developed in TSA-Net [37].

Evaluation Metrics. We choose peak signal-to-noise ratio (PSNR) [9] and structural similarity (SSIM) [60] as the evaluation metrics to assess the performance of HSI reconstruction.

Implementation Details. The PGDUDST model was implemented using the PyTorch framework and trained with the Adam optimizer, utilizing hyperparameters $\beta_1 = 0.9$ and $\beta_2 = 0.999$. The training process extended over 200 epochs, employing the cosine annealing scheduler with linear warm-up. The learning rate and batch size were set to 2×10^{-4} and 1, respectively. When performing experiments on simulated data, the networks were fed patches with a spatial size of 256×256 cropped from the 3D cubes. In the case of real HSI reconstruction, the patch size was adjusted to 660×660 to align with real-world measurements. The dispersion shift steps were configured as 2, and data augmentation techniques, including random flipping and rotation, were applied. The model aimed to minimize the Charbonnier loss.

4.2. Quantitative Results

In our study, we conducted a comprehensive comparative analysis of the proposed PGDUDST method and state-of-the-art (SOTA) HSI restoration techniques. We compared the results of PGDUDST with 15 SOTA methods, including three model-based methods (TwIST [3], GAP-TV [62], and DeSCI [32]), seven end-to-end methods (V-DUnet [13], λ -net [40], TSA-net [37], HDNet [23], MST [5], CST [4], and MST++ [6]), and five deep unfolding methods (ADMM-net [35], GAP-net [36], DGSM [25], DAUHST [7], and RDLUF-Mix S^2 [15]) across 10 simulation scenes. All techniques were trained using the same datasets and evaluated under identical settings as DGSM [25] to ensure fair comparisons.

The effectiveness of different methods was assessed based on the metrics of peak signal-to-noise ratio (PSNR) and structural similarity index (SSIM). The corresponding results for the 10 simulated scenes are presented in Table 1. From Table 1, it is evident that PGDUDST exhibits the best reconstruction performance, surpassing other approaches. Compared to λ -net [40], TSA-net [37], V-DUnet [13], GAP-net [36], HDNet [23], CST-L-plus [4], and RDLUF-Mix S^2 -9stg [15], the proposed method with 9 stages achieves significant improvements, with average gains of 11.29 dB, 8.36 dB, 7.78 dB, 6.56 dB, 4.85 dB, 3.7 dB, and 0.23 dB, respectively.

What stands out is that, although our network's average PSNR for reconstruction seems to be only 0.23 dB higher than that of RDLUF-Mix S^2 -9stg [15], we wish to emphasize that our network achieves comparable reconstruction results to RDLUF-Mix S^2 -9stg [15] while requiring only 58% of the training time. Additionally, it is crucial to highlight that our approach surpasses the network reconstruction performance limit of RDLUF-Mix S^2 . Detailed explanations for these two aspects will be provided in the following sections, namely "Comparison of Training Times with RDLUF-Mix S^2 " and "Comparative Analysis of Network Reconstruction Performance Limits with RDLUF-Mix S^2 ."

Comparison of Training Times with RDLUF-Mix S^2 . Considering that the original configuration of RDLUF-Mix S^2 [15] specified 300 epochs, we opted to train our model for an equivalent number of epochs. This decision facilitates a more intuitive comparison of the reconstruction PSNR and SSIM between the two methods. Furthermore, it ensures a

Table 1. Comparisons of PSNR (upper entry in each cell) and SSIM (lower entry in each cell) for different methods across 10 simulation scenes (S1-S10).

Algorithms	S1	S2	S3	S4	S5	S6	S7	S8	S9	S10	Avg
TwIST [3]	25.16 0.700	23.02 0.604	21.40 0.711	30.19 0.851	21.41 0.635	20.95 0.644	22.20 0.643	21.82 0.650	22.42 0.690	22.67 0.569	23.12 0.669
GAP-TV [62]	26.82 0.754	22.89 0.610	26.31 0.802	30.65 0.852	23.64 0.703	21.85 0.663	23.76 0.688	21.98 0.655	22.63 0.682	23.10 0.584	24.36 0.669
DeSCI [32]	27.13 0.748	23.04 0.620	26.62 0.818	34.96 0.897	23.94 0.706	22.38 0.683	24.45 0.743	22.03 0.673	24.56 0.732	23.59 0.587	25.27 0.721
λ -net [40]	30.10 0.849	28.49 0.805	27.73 0.870	37.01 0.934	26.19 0.817	28.64 0.853	26.47 0.806	26.09 0.831	27.50 0.826	27.13 0.816	28.53 0.841
TSA-Net [37]	32.03 0.892	31.00 0.858	32.25 0.915	39.19 0.953	29.39 0.884	31.44 0.908	30.32 0.878	29.35 0.888	30.01 0.890	29.59 0.874	31.46 0.894
V-DUnet [13]	32.70 0.892	32.21 0.891	32.91 0.933	39.01 0.956	30.10 0.910	31.45 0.914	31.00 0.885	29.78 0.900	31.62 0.897	29.64 0.873	32.04 0.905
DGSMP [25]	33.26 0.915	32.09 0.898	33.06 0.925	40.54 0.964	28.86 0.882	33.08 0.937	30.74 0.886	31.35 0.923	31.66 0.911	31.44 0.925	32.63 0.917
GAP-Net [36]	33.74 0.911	33.26 0.900	34.28 0.929	41.03 0.967	31.44 0.919	32.40 0.925	32.27 0.902	30.46 0.905	33.51 0.915	30.24 0.895	33.26 0.917
ADMM-Net [35]	34.12 0.918	33.62 0.906	35.04 0.931	41.15 0.966	31.82 0.922	32.54 0.924	32.42 0.896	30.74 0.907	33.75 0.915	30.68 0.895	33.58 0.918
HDnet [23]	35.14 0.935	35.67 0.940	36.03 0.943	42.30 0.969	32.69 0.946	34.46 0.952	33.67 0.926	32.48 0.941	34.89 0.942	32.38 0.937	34.97 0.943
MST-L [5]	35.40 0.941	35.87 0.944	36.51 0.953	42.27 0.973	32.77 0.947	34.80 0.955	33.66 0.925	32.67 0.948	35.39 0.949	32.50 0.941	35.18 0.948
MST++ [6]	35.80 0.943	36.23 0.947	37.34 0.957	42.63 0.973	33.38 0.952	35.38 0.957	34.35 0.934	33.71 0.953	36.67 0.953	33.38 0.945	35.99 0.951
CST-L* [4]	35.96 0.949	36.84 0.955	38.16 0.962	42.44 0.975	33.25 0.955	35.72 0.963	34.86 0.944	34.34 0.961	36.51 0.957	33.09 0.945	36.12 0.957
DAUHST-9stg [7]	37.25 0.958	39.02 0.967	41.05 0.971	46.15 0.983	35.80 0.969	37.08 0.970	37.57 0.963	35.10 0.966	40.02 0.970	34.59 0.956	38.36 0.967
RDLUF-MixS ² -5stg [15]	37.30 0.960	39.39 0.971	42.06 0.975	46.89 0.988	35.74 0.969	37.03 0.971	37.05 0.959	35.18 0.968	40.64 0.973	34.58 0.957	38.59 0.969
RDLUF-MixS ² -7stg [15]	37.65 0.963	40.45 0.976	43.00 0.978	47.40 0.990	36.78 0.974	37.56 0.974	38.25 0.967	35.86 0.971	41.71 0.978	34.83 0.959	39.35 0.973
RDLUF-MixS ² -9stg [15]	37.94 0.966	40.95 0.977	43.25 0.979	47.83 0.990	37.11 0.976	37.47 0.975	38.58 0.969	35.50 0.970	41.83 0.978	35.23 0.962	39.57 0.974
Ours 5stage	37.49 0.964	40.22 0.975	42.68 0.978	47.30 0.988	36.11 0.972	37.12 0.972	38.08 0.966	35.46 0.969	41.38 0.977	34.99 0.961	39.08 0.972
Ours 7stage	37.89 0.965	40.90 0.978	43.34 0.979	47.64 0.990	36.60 0.976	37.46 0.975	38.46 0.969	36.14 0.974	42.28 0.979	35.15 0.962	39.59 0.974
Ours 9stage	37.90 0.966	41.22 0.979	43.55 0.980	47.87 0.990	37.25 0.977	37.62 0.975	38.92 0.969	36.28 0.973	42.53 0.980	35.06 0.961	39.82 0.975

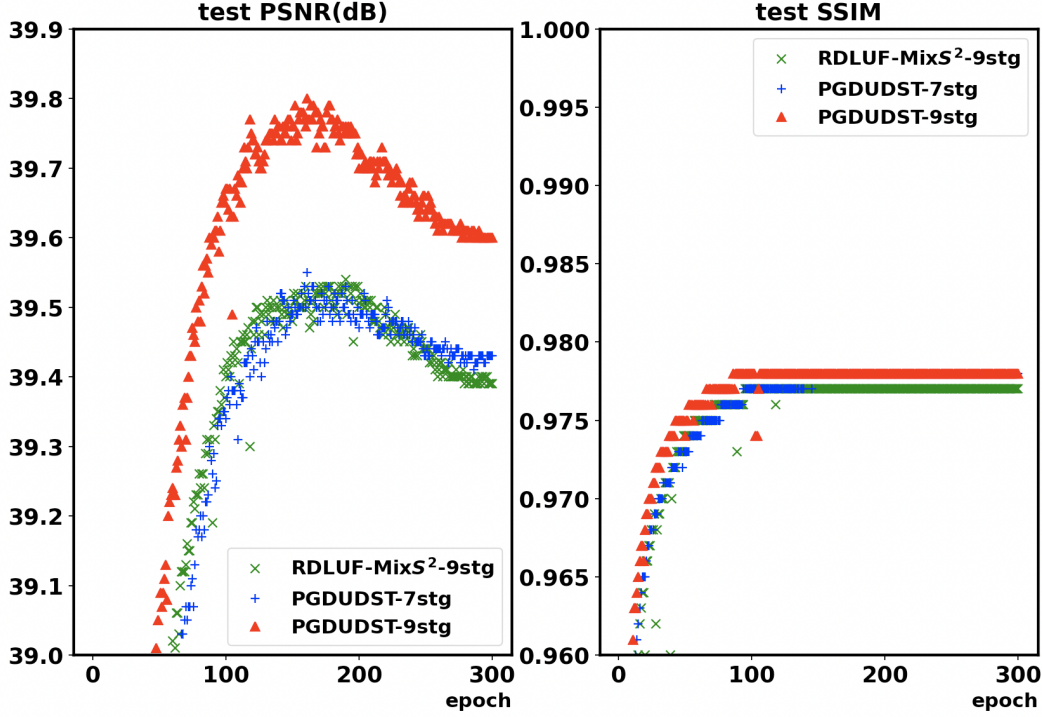


Figure 5. Comparison of PSNR and SSIM for the models RDLUF-Mix S^2 -9stage, PGDUDST-7stage, and PGDUDST-9stage on 10 simulated test images.

fair evaluation of training duration, enhancing the comparability of our visualization results. It is important to emphasize, however, that our approach only requires setting epochs to 200.

The reason our PGDUDST only requires 200 epochs, instead of being set to 300 epochs like RDLUF-Mix S^2 [15], can be found in Figure 5. As depicted in the figure, our PGDUDST, including both PGDUDST-7stg and PGDUDST-9stg, converges to the best PSNR value around epoch 150. In contrast, RDLUF-Mix S^2 [15] reaches its best PSNR value around epoch 200. This indicates that the convergence speed of our PGDUDST is much faster than that of RDLUF-Mix S^2 [15]. Consequently, we can significantly reduce the number of training epochs to 200. Additionally, since RDLUF-Mix S^2 [15] converges to its best PSNR value around epoch 200, setting the epochs for RDLUF-Mix S^2 [15] to 200 might be risky, as it may not converge to the best reconstruction result within 200 epochs.

From Figure 5, we observe that our PGDUDST-7stg can achieve reconstruction results comparable to those of RDLUF-Mix S^2 -9stg. Strictly speaking, it even outperforms RDLUF-Mix S^2 -9stg. Consequently, we conducted a detailed comparison of the training duration required for PGDUDST-7stg (which can achieve reconstruction results comparable to RDLUF-Mix S^2 -9stg) and RDLUF-Mix S^2 -9stg (which achieved the best reconstruction results of RDLUF-Mix S^2). RDLUF-Mix S^2 -9stg requires a total training time of 339.3 hours for 300 epochs, approximately 14.1 days. In contrast, PGDUDST-7stg requires 293.5 hours for 300 epochs, approximately 12.2 days. Even with the training epochs set to 300, PGDUDST-7stg still outperforms RDLUF-Mix S^2 -9stg in terms of time efficiency, saving approximately 14% of the total training time while maintaining comparable results to RDLUF-Mix S^2 -9stg.

Due to the rapid convergence of our network, setting the epochs to 300 is unnecessary; we believe that setting PGDUDST's epochs to 200 is sufficient. PGDUDST-7stg requires 197.7 hours for 200 epochs, approximately 8.2 days. This results in a 42% reduction in our network's training time. In summary, PGDUDST-7stg requires only 58% of the training time compared to RDLUF-Mix S^2 -9stg, yet achieves comparable training reconstruction results. Moreover, as evident from Figure 5, PGDUDST-9stg outperforms RDLUF-Mix S^2 -9stg in training results. The training time required for 200 epochs of PGDUDST-9stg is only 256.1 hours, approximately 10.7 days. Compared to RDLUF-Mix S^2 -9stg, this represents a 25% reduction in training time, indicating that PGDUDST can achieve superior results in a shorter training period than RDLUF-Mix S^2 -9stg.

In summary, PGDUDST significantly shortens training time through two key mechanisms. Firstly, by alleviating the

computational burden on the network, we achieve a notable reduction in training time (even with 300 epochs of training, PGDUDST-7stg requires 14% less time than RDLUF-Mix S^2 -9stg). Secondly, by accelerating the convergence speed of the network, we further minimize training duration. PGDUDST’s convergence speed surpasses that of RDLUF-Mix S^2 [15], enabling us to reduce the number of training epochs and thus significantly reduce overall training time. In total, PGDUDST only requires 58% of the training time needed by RDLUF-Mix S^2 -9stg to achieve comparable reconstruction results.

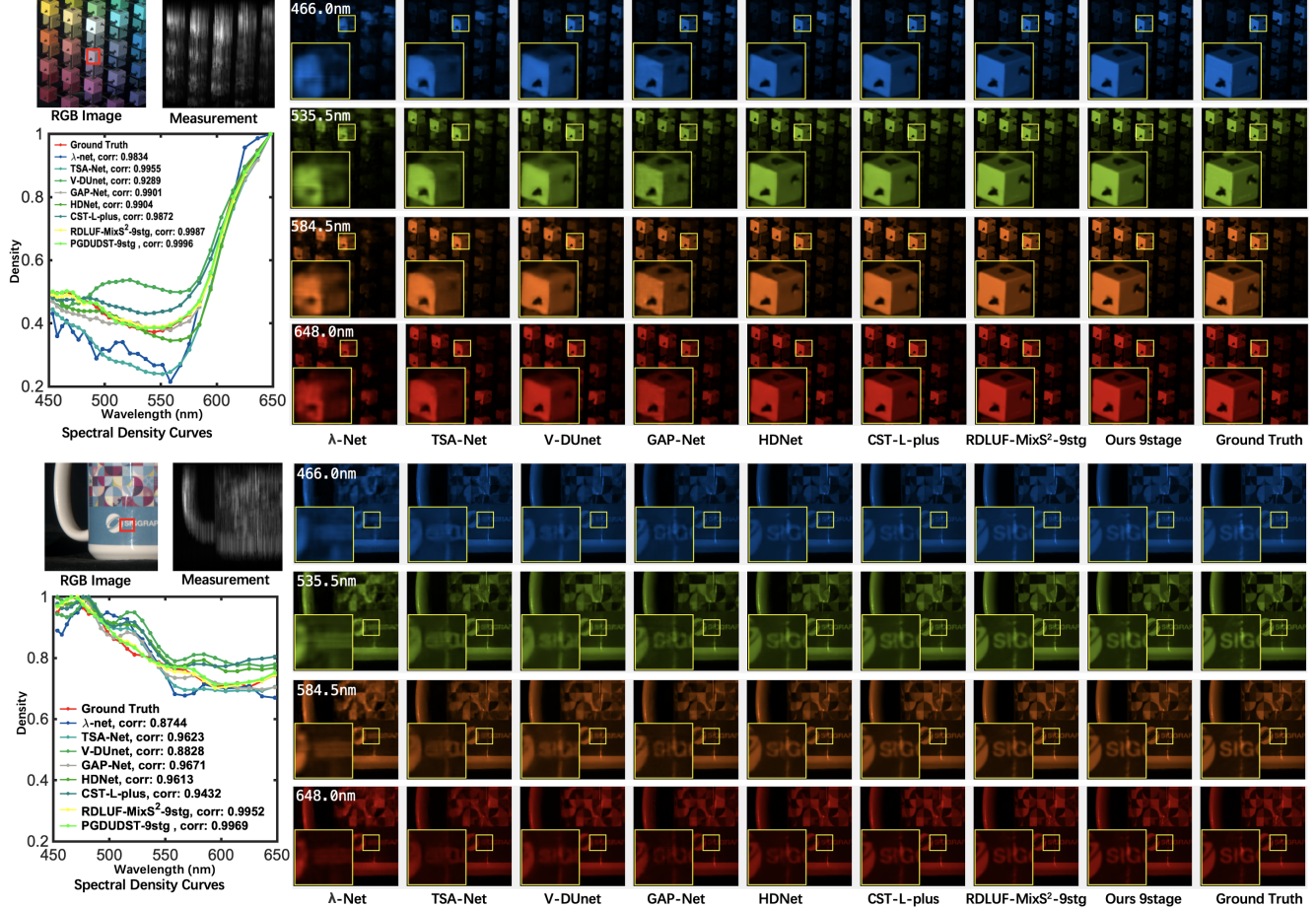


Figure 6. Comparisons of reconstructed simulation HSI for Scene 2 (top) and Scene 5 (bottom) using 4 out of 28 spectral channels are presented. The evaluation includes 7 SOTA algorithms alongside our PGDUDST-9stg method. The spectral curves correspond to the selected red box in the RGB image. Zoom in for a more detailed examination.

Comparative Analysis of Network Reconstruction Performance Limits with RDLUF-Mix S^2 . The reconstructed performance of both PGDUDST and RDLUF-Mix S^2 [15] was further compared by increasing the stage number to 11 and training PGDUDST-11stg and RDLUF-Mix S^2 -11stg.

The corresponding best reconstruction results for PGDUDST-11stg and RDLUF-Mix S^2 -11stg are outlined in Table 2. A closer examination of Table 2 reveals that the reconstruction outcomes of PGDUDST-11stg are marginally inferior to those of PGDUDST-9stg. Similarly, the reconstruction results of RDLUF-Mix S^2 -11stg are somewhat worse than those of RDLUF-Mix S^2 -9stg. This observation suggests that, irrespective of whether it is PGDUDST or RDLUF-Mix S^2 [15], the reconstruction results do not unconditionally improve with an increase in the stage number; instead, they may experience some weakening. In essence, the reconstruction performance of both PGDUDST and RDLUF-Mix S^2 has its limitations. Referring to Table 1 and Table 2, we can draw the following conclusions: PGDUDST-9stg and RDLUF-Mix S^2 -9stg serve as the respective network reconstruction performance limits for PGDUDST and RDLUF-Mix S^2 . Moreover, it is evident that the reconstruction limit of PGDUDST exceeds that of RDLUF-Mix S^2 , implying that our proposed PGDUDST surpasses the network’s reconstruction limit of RDLUF-Mix S^2 .

Simulation HSI Reconstruction. We present a comparison of the proposed PGDUDST method for HSI reconstruction,

Table 2. Comparison of PSNR (upper entry in each cell) and SSIM (lower entry in each cell) across 10 simulation scenes (S1-S10) with RDLUF-Mix S^2 -9stg, RDLUF-Mix S^2 -11stg, our 9stage, and our 11stage models.

IMP	S1	S2	S3	S4	S5	S6	S7	S8	S9	S10	Avg
RDLUF-Mix S^2 -9stg	37.94	40.95	43.25	47.83	37.11	37.47	38.58	35.50	41.83	35.23	39.57
	0.966	0.977	0.979	0.990	0.976	0.975	0.969	0.970	0.978	0.962	0.974
RDLUF-Mix S^2 -11stg	37.73	40.89	43.33	47.38	36.86	37.47	38.82	35.77	41.81	35.13	39.52
	0.965	0.978	0.979	0.989	0.976	0.974	0.970	0.972	0.978	0.962	0.974
Ours 9stage	37.90	41.22	43.55	47.87	37.25	37.62	38.92	36.28	42.53	35.06	39.82
	0.966	0.979	0.980	0.990	0.977	0.975	0.969	0.973	0.980	0.961	0.975
Ours 11stage	37.84	41.24	43.18	47.68	37.55	37.71	38.86	36.10	42.43	35.21	39.78
	0.966	0.980	0.979	0.989	0.979	0.976	0.970	0.974	0.980	0.962	0.975

utilizing 4 out of 28 spectral channels from Scene 2 and Scene 5, against the simulation results obtained from seven SOTA approaches. Displayed in Fig. 6, our method yields visually smoother and cleaner textures while retaining the spatial information of homogeneous regions. The results emphasize the effectiveness of our approach in producing high-quality HSIs with improved texture characteristics and preserved spatial information. Specifically, our method leverages the Spectral-attention branch to effectively model long-range dependencies and enhances the capability to capture detailed textures through the Dense-spatial branch. Additionally, we validate the spectral consistency of our approach by comparing the spectral density curves of the reconstructed areas with the actual ground truth. As shown in the bottom-left of each scene in Fig. 6, our method achieved the highest correlation coefficient, emphasizing the effectiveness of our proposed method.

Real HSI Reconstruction. We retrained our model on the CAVE [43] and KAIST [14] datasets, conducting tests on real measurements to implement actual experiments, following the configurations established in previous works [4, 5, 15, 25, 37]. To simulate real measurement conditions, we introduced 11-bit shot noise during the training process. As depicted in Fig. 7, we conducted a comparative analysis of the reconstructed images from two real scenes (Scene 2 and Scene 3) using our PGDUDST method and seven SOTA approaches. Our model achieved competitive results when compared to SOTA methods. Notably, in Scene 2, it is evident that the proposed method excels in restoring more texture and detail. In Scene 3, the faces reconstructed by our approach exhibit exceptional clarity. Unlike other methods, our solution avoids generating non-existent features such as noses or forehead wrinkles and minimizes the presence of other artifacts. Notably, our approach is unique in accurately reconstructing the two distinct curves representing the lips, a detail that remains indiscernible in the reconstructions produced by alternative methods. Moreover, our reconstruction of the right eye provides a clearer depiction, offering enhanced visibility of the eyebrows. Overall, in terms of the reconstructed images, our approach markedly reduces the problem of artifacts present in other solutions, achieving reconstructions that are cleaner and more defined in detail.

5. Conclusion

In conclusion, this study introduces the Dense-spatial Spectral-attention Transformer (DST) into the Proximal Gradient Descent Unfolding Framework (PGDUF) and proposes a novel approach called Proximal Gradient Descent Unfolding Dense-spatial Spectral-attention Transformer (PGDUDST) for the reconstruction of hyperspectral images. This method effectively addresses two major flaws in the RDLUF-Mix S^2 network. First, the substantial computational burden of RDLUF-Mix S^2 results in excessively long training times. Second, RDLUF-Mix S^2 exhibits poor performance on real experimental data, leading to significant artifacts in the reconstructed results.

PGDUDST successfully overcomes these challenges. Firstly, it achieves reconstruction results comparable to RDLUF-Mix S^2 -9stg but with only 58% of the training time required by RDLUF-Mix S^2 -9stg. Secondly, PGDUDST surpasses the reconstruction limits of RDLUF-Mix S^2 , obtaining superior results. Lastly, PGDUDST demonstrates outstanding performance on real experimental data, effectively mitigating numerous artifacts present in the reconstructed images generated by RDLUF-Mix S^2 . These results underscore the efficiency and effectiveness of PGDUDST in hyperspectral image reconstruction, showcasing its potential to accelerate convergence and improve adaptability in real-world scenarios. The proposed method holds promise for advancing the practical applications of hyperspectral imaging technology in various fields, including medical imaging, remote sensing, and target tracking.

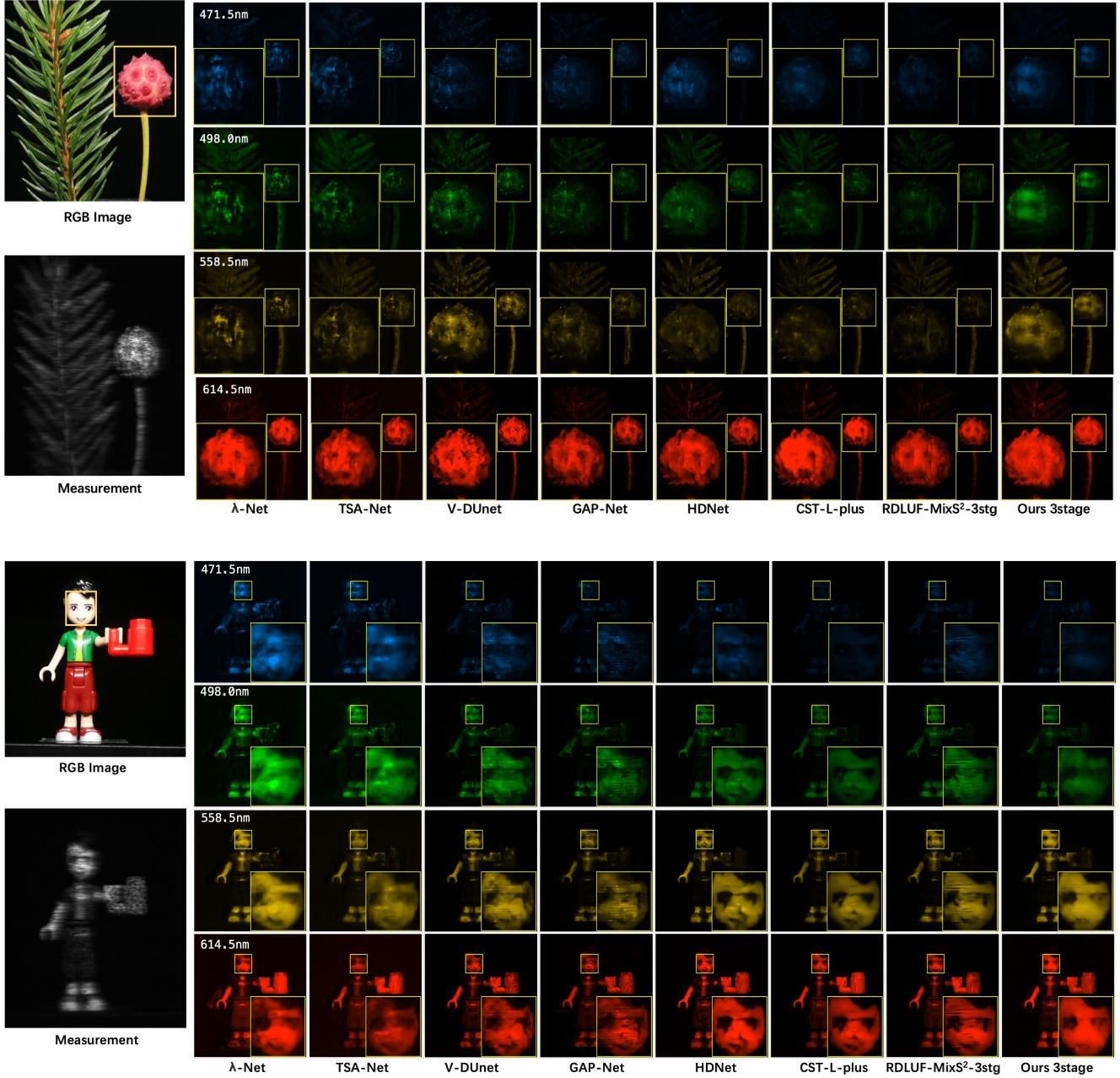


Figure 7. Comparative Reconstruction of Real HSI: Scenes 2 and 3. Four spectra were randomly selected from a total of 28.

References

- [1] Gonzalo R. Arce, David J. Brady, Lawrence Carin, Henry Arguello, and David S. Kittle. Compressive coded aperture spectral imaging: An introduction. *IEEE Signal Processing Magazine*, 31(1):105–115, 2014. 1
- [2] Amir Beck and Marc Teboulle. A fast iterative shrinkage-thresholding algorithm for linear inverse problems. *SIAM journal on imaging sciences*, 2(1):183–202, 2009. 2
- [3] JosÉ M. Bioucas-Dias and Mário A. T. Figueiredo. A new twist: Two-step iterative shrinkage/thresholding algorithms for image restoration. *IEEE Transactions on Image Processing*, 16(12):2992–3004, 2007. 8, 9
- [4] Yuanhao Cai, Jing Lin, Xiaowan Hu, Haoqian Wang, Xin Yuan, Yulun Zhang, Radu Timofte, and Luc Van Gool. Coarse-to-fine sparse transformer for hyperspectral image reconstruction. In *ECCV*, 2022. 1, 8, 9, 12
- [5] Yuanhao Cai, Jing Lin, Xiaowan Hu, Haoqian Wang, Xin Yuan, Yulun Zhang, Radu Timofte, and Luc Van Gool. Mask-guided

- spectral-wise transformer for efficient hyperspectral image reconstruction. In *CVPR*, 2022. 1, 7, 8, 9, 12
- [6] Yuanhao Cai, Jing Lin, Zudi Lin, Haoqian Wang, Yulun Zhang, Hanspeter Pfister, Radu Timofte, and Luc Van Gool. Mst++: Multi-stage spectral-wise transformer for efficient spectral reconstruction. In *Proceedings of the IEEE/CVF Conference on Computer Vision and Pattern Recognition (CVPR) Workshops*, pages 745–755, 2022. 8, 9
 - [7] Yuanhao Cai, Jing Lin, Haoqian Wang, Xin Yuan, Henghui Ding, Yulun Zhang, Radu Timofte, and Luc Van Gool. Degradation-aware unfolding half-shuffle transformer for spectral compressive imaging. *arXiv preprint arXiv:2205.10102*, 2022. 1, 8, 9
 - [8] Xun Cao, Tao Yue, Xing Lin, Stephen Lin, Xin Yuan, Qionghai Dai, Lawrence Carin, and David J Brady. Computational snapshot multispectral cameras: Toward dynamic capture of the spectral world. *IEEE Signal Processing Magazine*, 33(5):95–108, 2016. 1
 - [9] Luen C. Chan and Peter Whiteman. Hardware-constrained hybrid coding of video imagery. *IEEE Transactions on Aerospace and Electronic Systems*, AES-19(1):71–84, 1983. 8
 - [10] Stanley H Chan, Xiran Wang, and Omar A Elgendy. Plug-and-play admm for image restoration: Fixed-point convergence and applications. *IEEE Transactions on Computational Imaging*, 3(1):84–98, 2016. 1, 4
 - [11] Qiang Chen, Qiman Wu, Jian Wang, Qinghao Hu, Tao Hu, Errui Ding, Jian Cheng, and Jingdong Wang. Mixformer: Mixing features across windows and dimensions. In *Proceedings of the IEEE/CVF conference on computer vision and pattern recognition*, pages 5249–5259, 2022. 7
 - [12] Wenwu Chen, Bo Zhang, Liuning Gu, Haibo Liu, Jinli Suo, and Xinxing Shao. Snapshot compressive imaging based digital image correlation: temporally super-resolved full-resolution deformation measurement. *Optics Express*, 30(19):33554–33573, 2022. 1
 - [13] Ziyang Chen, Zhentao Liu, Chenyu Hu, Heng Wu, Jianrong Wu, Jinda Lin, Zhishen Tong, Hong Yu, and Shensheng Han. Hyper-spectral image reconstruction for spectral camera based on ghost imaging via sparsity constraints using v-dunet. *arXiv preprint arXiv:2206.14199*, 2022. 8, 9
 - [14] Inchang Choi, MH Kim, D Gutierrez, DS Jeon, and G Nam. High-quality hyperspectral reconstruction using a spectral prior. Technical report, 2017. 8, 12
 - [15] Yubo Dong, Dahua Gao, Tian Qiu, Yuyan Li, Minxi Yang, and Guangming Shi. Residual degradation learning unfolding framework with mixing priors across spectral and spatial for compressive spectral imaging. In *Proceedings of the IEEE/CVF Conference on Computer Vision and Pattern Recognition*, pages 22262–22271, 2023. 1, 2, 4, 7, 8, 9, 10, 11, 12
 - [16] Hao Du, Xin Tong, Xun Cao, and Stephen Lin. A prism-based system for multispectral video acquisition. In *2009 IEEE 12th International Conference on Computer Vision*, pages 175–182. IEEE, 2009. 1
 - [17] Mário AT Figueiredo, Robert D Nowak, and Stephen J Wright. Gradient projection for sparse reconstruction: Application to compressed sensing and other inverse problems. *IEEE Journal of selected topics in signal processing*, 1(4):586–597, 2007. 1
 - [18] Ying Fu, Zhiyuan Liang, and Shaodi You. Bidirectional 3d quasi-recurrent neural network for hyperspectral image super-resolution. *IEEE Journal of Selected Topics in Applied Earth Observations and Remote Sensing*, 14:2674–2688, 2021. 1
 - [19] Liang Gao and R Theodore Smith. Optical hyperspectral imaging in microscopy and spectroscopy—a review of data acquisition. *Journal of biophotonics*, 8(6):441–456, 2015. 1
 - [20] Michael E Gehm, Renu John, David J Brady, Rebecca M Willett, and Timothy J Schulz. Single-shot compressive spectral imaging with a dual-disperser architecture. *Optics express*, 15(21):14013–14027, 2007. 1
 - [21] Yanfeng Gu, Tianzhu Liu, Guoming Gao, Guangbo Ren, Yi Ma, Jocelyn Chanussot, and Xiuping Jia. Multimodal hyperspectral remote sensing: An overview and perspective. *Science China Information Sciences*, 64:1–24, 2021. 1
 - [22] Jie Hu, Li Shen, and Gang Sun. Squeeze-and-excitation networks. In *Proceedings of the IEEE conference on computer vision and pattern recognition*, pages 7132–7141, 2018. 7
 - [23] Xiaowan Hu, Yuanhao Cai, Jing Lin, Haoqian Wang, Xin Yuan, Yulun Zhang, Radu Timofte, and Luc Van Gool. Hdnet: High-resolution dual-domain learning for spectral compressive imaging. In *CVPR*, 2022. 1, 8, 9
 - [24] Gao Huang, Zhuang Liu, Laurens van der Maaten, and Kilian Q. Weinberger. Densely connected convolutional networks. In *Proceedings of the IEEE Conference on Computer Vision and Pattern Recognition (CVPR)*, pages 4700–4708, 2017. 7
 - [25] Tao Huang, Weisheng Dong, Xin Yuan, Jinjian Wu, and Guangming Shi. Deep gaussian scale mixture prior for spectral compressive imaging. In *Proceedings of the IEEE/CVF Conference on Computer Vision and Pattern Recognition (CVPR)*, pages 16216–16225, 2021. 1, 8, 9, 12
 - [26] Tao Huang, Weisheng Dong, Xin Yuan, Jinjian Wu, and Guangming Shi. Deep gaussian scale mixture prior for spectral compressive imaging. In *Proceedings of the IEEE/CVF Conference on Computer Vision and Pattern Recognition*, pages 16216–16225, 2021. 1
 - [27] Maryam Imani and Hassan Ghassemian. An overview on spectral and spatial information fusion for hyperspectral image classification: Current trends and challenges. *Information fusion*, 59:59–83, 2020. 1
 - [28] Shahid Karim, Akeel Qadir, Umar Farooq, Muhammad Shakir, and Asif A Laghari. Hyperspectral imaging: a review and trends towards medical imaging. *Current Medical Imaging*, 19(5):417–427, 2023. 1
 - [29] David Kittle, Kerkil Choi, Ashwin Wagadarikar, and David J Brady. Multiframe image estimation for coded aperture snapshot spectral imagers. *Applied optics*, 49(36):6824–6833, 2010. 1
 - [30] Asif Ali Laghari, S Yin, et al. How to collect and interpret medical pictures captured in highly challenging environments that range from nanoscale to hyperspectral imaging. *Current Medical Imaging*, 54:36582065, 2022. 1

- [31] Zhuanfeng Li, Fengchao Xiong, Jun Zhou, Jing Wang, Jianfeng Lu, and Yuntao Qian. Bae-net: A band attention aware ensemble network for hyperspectral object tracking. In *2020 IEEE international conference on image processing (ICIP)*, pages 2106–2110. IEEE, 2020. 1
- [32] Yang Liu, Xin Yuan, Jinli Suo, David J Brady, and Qionghai Dai. Rank minimization for snapshot compressive imaging. *IEEE transactions on pattern analysis and machine intelligence*, 41(12):2990–3006, 2018. 1, 8, 9
- [33] Patrick Llull, Xuejun Liao, Xin Yuan, Jianbo Yang, David Kittle, Lawrence Carin, Guillermo Sapiro, and David J Brady. Coded aperture compressive temporal imaging. *Optics express*, 21(9):10526–10545, 2013. 1
- [34] Wenjing Lv and Xiaofei Wang. Overview of hyperspectral image classification. *Journal of Sensors*, 2020, 2020. 1
- [35] Jiawei Ma, Xiao-Yang Liu, Zheng Shou, and Xin Yuan. Deep tensor admm-net for snapshot compressive imaging. In *Proceedings of the IEEE/CVF International Conference on Computer Vision (ICCV)*, 2019. 1, 8, 9
- [36] Ziyi Meng, Shirin Jalali, and Xin Yuan. Gap-net for snapshot compressive imaging. *arXiv preprint arXiv:2012.08364*, 2020. 1, 8, 9
- [37] Ziyi Meng, Jiawei Ma, and Xin Yuan. End-to-end low cost compressive spectral imaging with spatial-spectral self-attention. In *European conference on computer vision*, pages 187–204. Springer, 2020. 1, 8, 9, 12
- [38] Ziyi Meng, Mu Qiao, Jiawei Ma, Zhenming Yu, Kun Xu, and Xin Yuan. Snapshot multispectral endomicroscopy. *Optics Letters*, 45(14):3897–3900, 2020. 1
- [39] Ziyi Meng, Zhenming Yu, Kun Xu, and Xin Yuan. Self-supervised neural networks for spectral snapshot compressive imaging. In *Proceedings of the IEEE/CVF international conference on computer vision*, pages 2622–2631, 2021. 1
- [40] Xin Miao, Xin Yuan, Yunchen Pu, and Vassilis Athitsos. l-net: Reconstruct hyperspectral images from a snapshot measurement. In *Proceedings of the IEEE/CVF International Conference on Computer Vision*, pages 4059–4069, 2019. 1, 8, 9
- [41] Chong Mou, Qian Wang, and Jian Zhang. Deep generalized unfolding networks for image restoration. In *Proceedings of the IEEE/CVF Conference on Computer Vision and Pattern Recognition (CVPR)*, pages 17399–17410, 2022. 4
- [42] Chaitanya B Pande and Kanak N Moharir. Application of hyperspectral remote sensing role in precision farming and sustainable agriculture under climate change: A review. *Climate Change Impacts on Natural Resources, Ecosystems and Agricultural Systems*, pages 503–520, 2023. 1
- [43] Jong-Il Park, Moon-Hyun Lee, Michael D Grossberg, and Shree K Nayar. Multispectral imaging using multiplexed illumination. In *2007 IEEE 11th International Conference on Computer Vision*, pages 1–8. IEEE, 2007. 8, 12
- [44] Taesung Park, Ming-Yu Liu, Ting-Chun Wang, and Jun-Yan Zhu. Semantic image synthesis with spatially-adaptive normalization. In *Proceedings of the IEEE/CVF conference on computer vision and pattern recognition*, pages 2337–2346, 2019. 4
- [45] Sima Peyghambari and Yun Zhang. Hyperspectral remote sensing in lithological mapping, mineral exploration, and environmental geology: an updated review. *Journal of Applied Remote Sensing*, 15(3):031501–031501, 2021. 1
- [46] Mu Qiao, Xuan Liu, and Xin Yuan. Snapshot spatial-temporal compressive imaging. *Optics letters*, 45(7):1659–1662, 2020. 1
- [47] Christian Szegedy, Vincent Vanhoucke, Sergey Ioffe, Jon Shlens, and Zbigniew Wojna. Rethinking the inception architecture for computer vision. In *Proceedings of the IEEE conference on computer vision and pattern recognition*, pages 2818–2826, 2016. 6
- [48] Christian Szegedy, Sergey Ioffe, Vincent Vanhoucke, and Alexander Alemi. Inception-v4, inception-resnet and the impact of residual connections on learning. In *Proceedings of the AAAI conference on artificial intelligence*, 2017. 6
- [49] Jin Tan, Yanting Ma, Hoover Rueda, Dror Baron, and Gonzalo R Arce. Compressive hyperspectral imaging via approximate message passing. *IEEE Journal of Selected Topics in Signal Processing*, 10(2):389–401, 2015. 1
- [50] Yiming Tang, Yufei Liu, Ling Ji, and Hong Huang. Robust hyperspectral object tracking by exploiting background-aware spectral information with band selection network. *IEEE Geoscience and Remote Sensing Letters*, 19:1–5, 2022. 1
- [51] Anton Terentev, Viktor Dolzhenko, Alexander Fedotov, and Danila Eremenko. Current state of hyperspectral remote sensing for early plant disease detection: A review. *Sensors*, 22(3):757, 2022. 1
- [52] Aziz ul Rehman and Shahzad Ahmad Qureshi. A review of the medical hyperspectral imaging systems and unmixing algorithms’ in biological tissues. *Photodiagnosis and Photodynamic Therapy*, 33:102165, 2021. 1
- [53] Ashwin Wagadarikar, Renu John, Rebecca Willett, and David Brady. Single disperser design for coded aperture snapshot spectral imaging. *Applied optics*, 47(10):B44–B51, 2008. 1
- [54] Ashwin A Wagadarikar, Nikos P Pitsianis, Xiaobai Sun, and David J Brady. Video rate spectral imaging using a coded aperture snapshot spectral imager. *Optics express*, 17(8):6368–6388, 2009. 1
- [55] Naftaly Wambugu, Yiping Chen, Zhenlong Xiao, Kun Tan, Mingqiang Wei, Xiaoxue Liu, and Jonathan Li. Hyperspectral image classification on insufficient-sample and feature learning using deep neural networks: A review. *International Journal of Applied Earth Observation and Geoinformation*, 105:102603, 2021. 1
- [56] Lizhi Wang, Zhiwei Xiong, Dahua Gao, Guangming Shi, Wenjun Zeng, and Feng Wu. High-speed hyperspectral video acquisition with a dual-camera architecture. In *Proceedings of the IEEE Conference on Computer Vision and Pattern Recognition*, pages 4942–4950, 2015. 1
- [57] Lizhi Wang, Zhiwei Xiong, Guangming Shi, Feng Wu, and Wenjun Zeng. Adaptive nonlocal sparse representation for dual-camera compressive hyperspectral imaging. *IEEE transactions on pattern analysis and machine intelligence*, 39(10):2104–2111, 2016. 1
- [58] Lizhi Wang, Chen Sun, Ying Fu, Min H Kim, and Hua Huang. Hyperspectral image reconstruction using a deep spatial-spectral prior. In *Proceedings of the IEEE/CVF Conference on Computer Vision and Pattern Recognition*, pages 8032–8041, 2019. 1

- [59] Lizhi Wang, Chen Sun, Maoqing Zhang, Ying Fu, and Hua Huang. Dnu: Deep non-local unrolling for computational spectral imaging. In *Proceedings of the IEEE/CVF Conference on Computer Vision and Pattern Recognition*, pages 1661–1671, 2020. [1](#)
- [60] Zhou Wang, A.C. Bovik, H.R. Sheikh, and E.P. Simoncelli. Image quality assessment: from error visibility to structural similarity. *IEEE Transactions on Image Processing*, 13(4):600–612, 2004. [8](#)
- [61] Fengchao Xiong, Jun Zhou, and Yuntao Qian. Material based object tracking in hyperspectral videos. *IEEE Transactions on Image Processing*, 29:3719–3733, 2020. [1](#)
- [62] Xin Yuan. Generalized alternating projection based total variation minimization for compressive sensing. In *2016 IEEE International conference on image processing (ICIP)*, pages 2539–2543. IEEE, 2016. [8](#), [9](#)
- [63] Xin Yuan, Yang Liu, Jinli Suo, and Qionghai Dai. Plug-and-play algorithms for large-scale snapshot compressive imaging. In *Proceedings of the IEEE/CVF Conference on Computer Vision and Pattern Recognition*, pages 1447–1457, 2020. [1](#), [4](#)
- [64] Xin Yuan, David J. Brady, and Aggelos K. Katsaggelos. Snapshot compressive imaging: Theory, algorithms, and applications. *IEEE Signal Processing Magazine*, 38(2):65–88, 2021. [1](#)
- [65] Xin Yuan, Yang Liu, Jinli Suo, Fredo Durand, and Qionghai Dai. Plug-and-play algorithms for video snapshot compressive imaging. *IEEE Transactions on Pattern Analysis and Machine Intelligence*, 44(10):7093–7111, 2021. [1](#)
- [66] Syed Waqas Zamir, Aditya Arora, Salman Khan, Munawar Hayat, Fahad Shahbaz Khan, and Ming-Hsuan Yang. Restormer: Efficient transformer for high-resolution image restoration. In *Proceedings of the IEEE/CVF conference on computer vision and pattern recognition*, pages 5728–5739, 2022. [6](#), [7](#)
- [67] Shipeng Zhang, Lizhi Wang, Ying Fu, Xiaoming Zhong, and Hua Huang. Computational hyperspectral imaging based on dimension-discriminative low-rank tensor recovery. In *Proceedings of the IEEE/CVF International Conference on Computer Vision*, pages 10183–10192, 2019. [1](#)
- [68] Xuanyu Zhang, Yongbing Zhang, Ruiqin Xiong, Qilin Sun, and Jian Zhang. Herosnet: Hyperspectral explicable reconstruction and optimal sampling deep network for snapshot compressive imaging. In *Proceedings of the IEEE/CVF Conference on Computer Vision and Pattern Recognition*, pages 17532–17541, 2022. [1](#)
- [69] Chunhui Zhao, Hongjiao Liu, Nan Su, Congan Xu, Yiming Yan, and Shou Feng. Tmtnet: A transformer-based multimodality information transfer network for hyperspectral object tracking. *Remote Sensing*, 15(4):1107, 2023. [1](#)